ARTICLE

OPEN

Check for updates

A glacier–ocean interaction model for tsunami genesis due to iceberg calving

Joshuah Wolper [1], Ming Gao[1,2], Martin P. Lüthi[3], Valentin Heller [4], Andreas Vieli [3], Chenfanfu Jiang[1] & Johan Gaume [5,6 ✉]

Glaciers calving icebergs into the ocean significantly contribute to sea-level rise and can trigger tsunamis, posing severe hazards for coastal regions. Computational modeling of such multiphase processes is a great challenge involving complex solid–fluid interactions. Here, a new continuum damage Material Point Method has been developed to model dynamic glacier fracture under the combined effects of gravity and buoyancy, as well as the subsequent propagation of tsunami-like waves induced by released icebergs. We reproduce the main features of tsunamis obtained in laboratory experiments as well as calving characteristics, the iceberg size, tsunami amplitude and wave speed measured at Eqip Sermia, an ocean-terminating outlet glacier of the Greenland ice sheet. Our hybrid approach constitutes important progress towards the modeling of solid–fluid interactions, and has the potential to contribute to refining empirical calving laws used in large-scale earth-system models as well as to improve hazard assessments and mitigation measures in coastal regions, which is essential in the context of climate change.

[1] University of Pennsylvania, Philadelphia, PA, USA. [2] Tencent Game AI Research Center, Los Angeles, CA, USA. [3] Department of Geography, University of Zürich, Zürich, Switzerland. [4] Environmental Fluid Mechanics and Geoprocesses Research Group, University of Nottingham, Nottingham, UK. [5] SLAB Snow and Avalanche Simulation Laboratory, EPFL Swiss Federal Institute of Technology, Lausanne, Switzerland. [6] WSL Institute for Snow and Avalanche Research SLF, Davos Dorf, Switzerland. ✉email: johan.gaume@epfl.ch

Glacier calving into the ocean (Fig. 1) is predicted to be one of the largest contributions to sea-level rise in the future[1–3]. This process corresponds to ~50% of the mass loss from ice sheets in Greenland and Antarctica[4,5]. Glacier calving is caused by first, second, and third-order processes. First-order processes correspond to the formation of surface crevasses in the ice owing to spatial variation in flow velocity. Second and third-order processes include crack propagation owing to local stress concentrations, ice stretching in the vicinity of the ice front, and oceanic erosion and torque induced by buoyant forces[6,7]. Depending on the shape of the glacier outlet, this may lead to different calving scenarios[8]. Glacier calving can have dramatic consequences, as falling or capsizing icebergs can generate large tsunamis, which are a threat to coastal infrastructure, ecology, and people[9–15]. In high mountain proglacial lakes, calving-induced waves may further pose major hazards through triggering lake outburst floods with high destructive potential in downstream valleys[16].

Most existing numerical approaches for marine-terminating glaciers were developed to study the slow creep of ice using continuum Eulerian methods (e.g., Elmer/Ice[17]), and the calving rate is generally evaluated using simplified and empirically based calving laws or simple analytic models[18]. In general, the validation of these models against observations remains relatively limited[19] and mostly excludes temporal scales of single calving events. Åström et al.[5,20] and Bassis and Jacobs[21] developed purely Lagrangian particle-based models, based on a discrete version of Newton's equations of motion, to study the dynamics of sea ice and glacier calving. Despite several approximations, including a simplified water–ice interaction law, their simulations were able to reproduce the fractal nature of the debris size distribution[20] and diverse calving features based on glacier geometry[21]. However, the discrete nature of these models makes them computationally very expensive and therefore limited to single events. Furthermore, the water in their simulation is not explicitly modeled, which prevents the study of the tsunamigenic potential of glacier calving. More recently, Mercenier et al.[22,23] developed a transient multiphysics finite element model to simulate the effect of oceanic melt on ice break-off at the terminus of a marine glacier. They showed that a von Mises stress criterion led to realistic calving front geometries. Although this model successfully couples slow glacier flow with a damage-based calving criterion, it cannot simulate tsunamis induced by calving.

Tsunamis generated by landslides were extensively studied[24,25]. Yet, only a few studies focused on tsunamis induced by calving glaciers. Lüthi and Vieli[10] reported a 45–50 m tsunami generated by the calving of a 200 m high ice cliff of the calving front of the Eqip Sermia glacier in Greenland. The wave was still 3.3 m large 4.5 km from the calving outlet and led to a 20 m run-up on the opposite shore. Recently, Heller et al.[13] performed large-scale laboratory experiments to study the characteristics of waves generated by different calving mechanisms. These authors showed that empirical equations established for landslides-induced tsunamis[25] overestimated wave amplitudes and generally fail to reproduce the physics of calving-induced tsunamis. Recently, Chen et al.[26] were able to reproduce the characteristics of waves reported in Heller et al.[13] using foam-extend and the Immersed Boundary Method. Yet, an approach to simulate fracture processes during dynamic glacier calving and tsunamis in a unified manner is still missing.

Here, we report coupled glacier calving and tsunami experiments and develop a continuum damage Material Point Method (MPM) to explicitly simulate ice fracture and hydraulic interactions. This new model accurately reproduces dynamic ice fractures and generated tsunami characteristics for different calving mechanisms for laboratory and real-world scales.

Results

Ice and water mechanics. To model the dynamic fracture of the glacier ice, we developed a non-associative elastoplastic model based on the Cohesive Cam Clay (CCC) yield surface used by Gaume et al.[27] to simulate snow and avalanche mechanics. A mixed-mode yield surface such as this was shown to adequately model brittle ice fracture based on experimental data[28]. However, the previously chosen associative flow rule was only adequate owing to the porous nature of snow, allowing for volume change (compaction hardening). Conversely, in the case of a significantly less-porous material such as ice, choosing a non-associative flow rule[29] is key owing to its natural volume-preserving qualities[30]. As such, we adopt a non-associative flow rule[31] coupled with a

Fig. 1 Calving event triggering a large tsunami. Kongsfjorden, Svalbard. [MB Photography]/[Moment] via Getty Images.
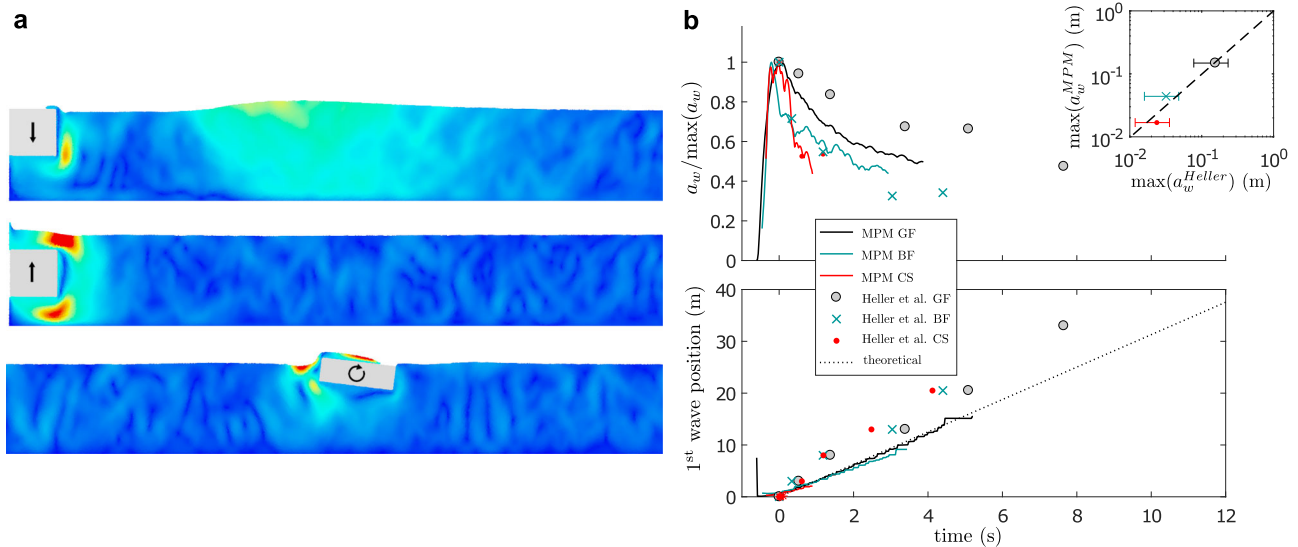
Fig. 2 Comparison between simulations and experiments of tsunamis generated by different calving mechanisms. a MPM simulations of a gravity-dominated fall of an iceberg (GF, top), buoyancy-dominated fall (BF, middle), and capsizing (CS, bottom) calving mechanisms. The color represents the velocity of water particles (blue = 0 m/s; red = 0.6 m/s). Movies of these three simulations can be found in the Supplement (Supplementary Movie 1). **b** (top) Amplitude of the first generated wave normalized by the maximum wave amplitude as a function of time. The inset shows the modeled maximum wave amplitude against the observed one from the laboratory experiments of Heller et al.[13], including error bars corresponding to uncertainties in the 2D/3D transformation (see Methods). Time was shifted so that the time corresponding to the maximum wave height corresponds to $t = 0$ s in all simulations and experiments. (Bottom) Position of the first generated wave as a function of time. The theoretical prediction for linear shallow-water waves is given by $x_{th} = \sqrt{gD_w}t$.

softening law to model the dynamic ice fracture. The mechanical behavior of water is simulated using a nearly incompressible equation of state[32]. The mass and momentum balance equations are solved numerically using the MPM[27,33] (see Methods for a complete model description).

Calving mechanism and tsunami wave characteristics. In a first set of experiments, we model the tsunami wave response to three main calving mechanisms according to the laboratory experiments of Heller et al.[13]: (i) gravity-dominated fall (GF), (ii) buoyancy-dominated fall (BF), and (iii) capsizing (CS). The numerical setup consists of the interaction between a rigid block of density similar to that of ice (920 kg/m³) and a $D_w = 1$ m deep water tank (see Methods) in two dimensions. For all simulated cases (Fig. 2 and Supplementary Movie 1), a rapid increase of the wave amplitude is reported until it reaches a maximum value. Then, the wave amplitude significantly decreases. A 2D/3D amplitude transformation factor based on an extensive amount of experimental data[34] (see Methods) was used to compare our results to those of Heller et al.[13]. A good agreement between our numerical solution and experimental data is observed. In particular, the maximum wave amplitude is correctly reproduced in both capsizing and gravity fall cases and slightly overestimated in the buoyant fall case (Fig. 2b). Concerning the wave velocity, our simulation results perfectly follow the theoretical limit prediction for linear shallow-water waves $v_w = \sqrt{gD_w}$; furthermore, a fair agreement with experimental data is reported. Consistent with laboratory experiments, our model results also suggest that gravity fall cases are the most hazardous as they induce the largest tsunami amplitudes.

Iceberg sizes: interplay between buoyancy and ice weight. To evaluate the capabilities of our new constitutive model for ice, we perform glacier calving MPM simulations using a simple geometry for which analytical solutions exist for validation: an ice block of height H_i is sliding at a constant velocity and enters a

water tank at varying submergence depth D to modify the buoyancy contribution and thus, ice fracture features. An example of simulation result for $D/H_i = 0.2$ is shown in Fig. 3a and Supplementary Movie 2. In this case, the main contribution to instability is gravity. Hence, we observe ice fractures starting to form at a certain length behind the front, and that propagate from the top of the glacier owing to gravity-induced bending. Once released, the iceberg generates a tsunami that propagates to the other side of the water tank (see Supplementary Movie 2). If the simulation is run for a long time, we observe subsequent detachments of icebergs of similar sizes, hence this length measure seems a robust output quantity of the model. The first iceberg length L_i is computed and plotted in Fig. 3b as a function of the submergence depth—ice height ratio D/H_i. The iceberg length first increases as submergence depth increases owing to a progressive stabilizing effect of buoyancy. For $D/H_i \sim 0.92 = \rho_i/\rho_w$, no ice failure is reported as the bending force due to the ice weight is compensated by the effect of buoyancy. For $D/H_i > 0.92$, we observe ice fractures starting from the bottom of the ice slab related to the effect of buoyant forces which overcome body weight forces. In turn, the iceberg length decreases with increasing D/H_i. Additional simulation results are shown in the Supplement for $D/H_i = 0.7$ and for lower ice strength values. Numerical results were then compared to a simple analytical model which compares the bending stress induced by the interplay between buoyancy and gravity and the ice tensile strength. This model (see Methods) leads to the following analytical expression for the iceberg length:

$$\frac{L_i}{H_i} = \left(\frac{2\sigma_t}{3\rho_i g H_i} \frac{1}{|1 - \frac{\rho_w}{\rho_i} \frac{D}{H_i}|} \right)^{\frac{1}{2}}, \tag{1}$$

where σ_t is the tensile strength of ice. Our MPM simulation results are in line with the predictions of this theoretical bending model (Fig. 3b) and are consistent with the position of the modeled stress maxima by Mercenier et al.[22].
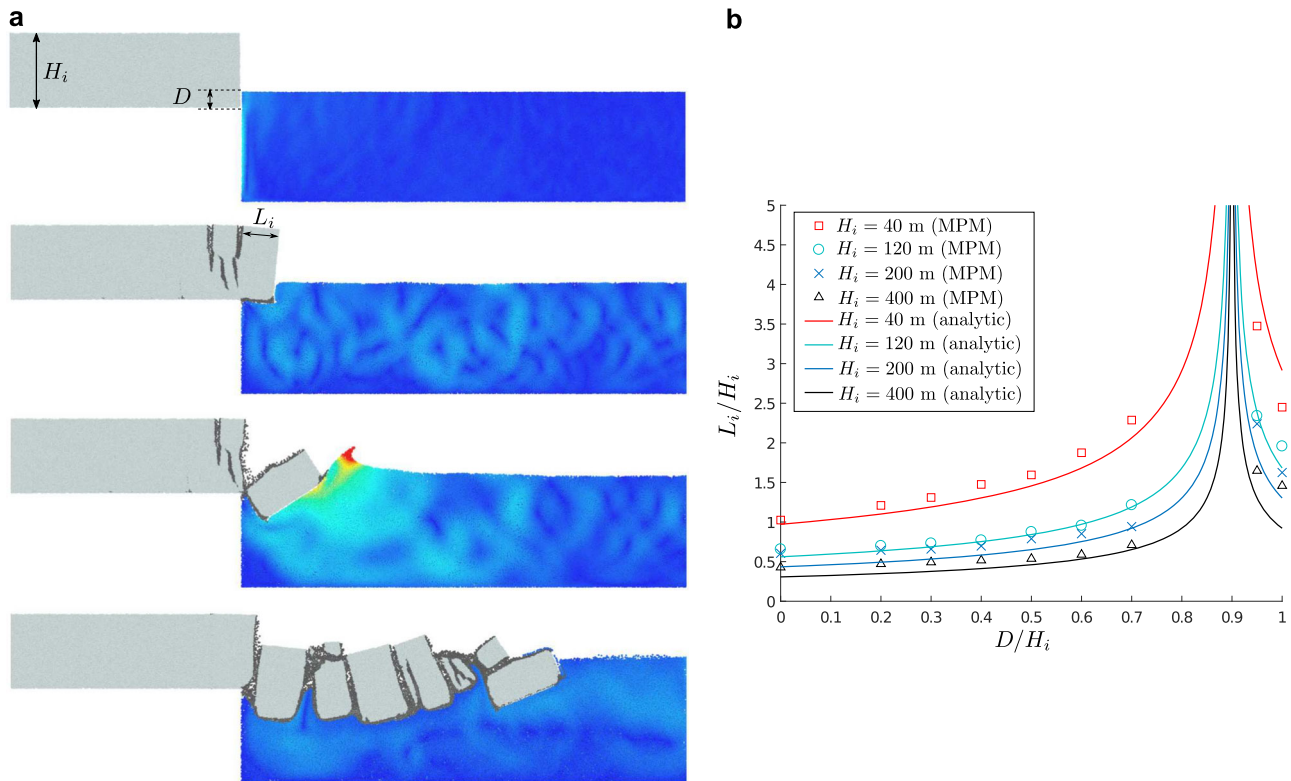
Fig. 3 Simulations of glacier calving and comparison with an analytical model for the iceberg length. a MPM simulations of glacier calving for $H_i = 200$ m and $D/H_i = 0.2$. A movie of this simulation can be found in the Supplement (Supplementary Movie 2). **b** Iceberg length to height ratio L_i/H_i as a function of the submergence depth to ice height ratio D/H_i. The analytical expression is given by Eq. (1). The water is colored by velocity: blue and red indicate water moving at 0 m/s and 20 m/s, respectively. The gray color in the glacier represents failed particles.
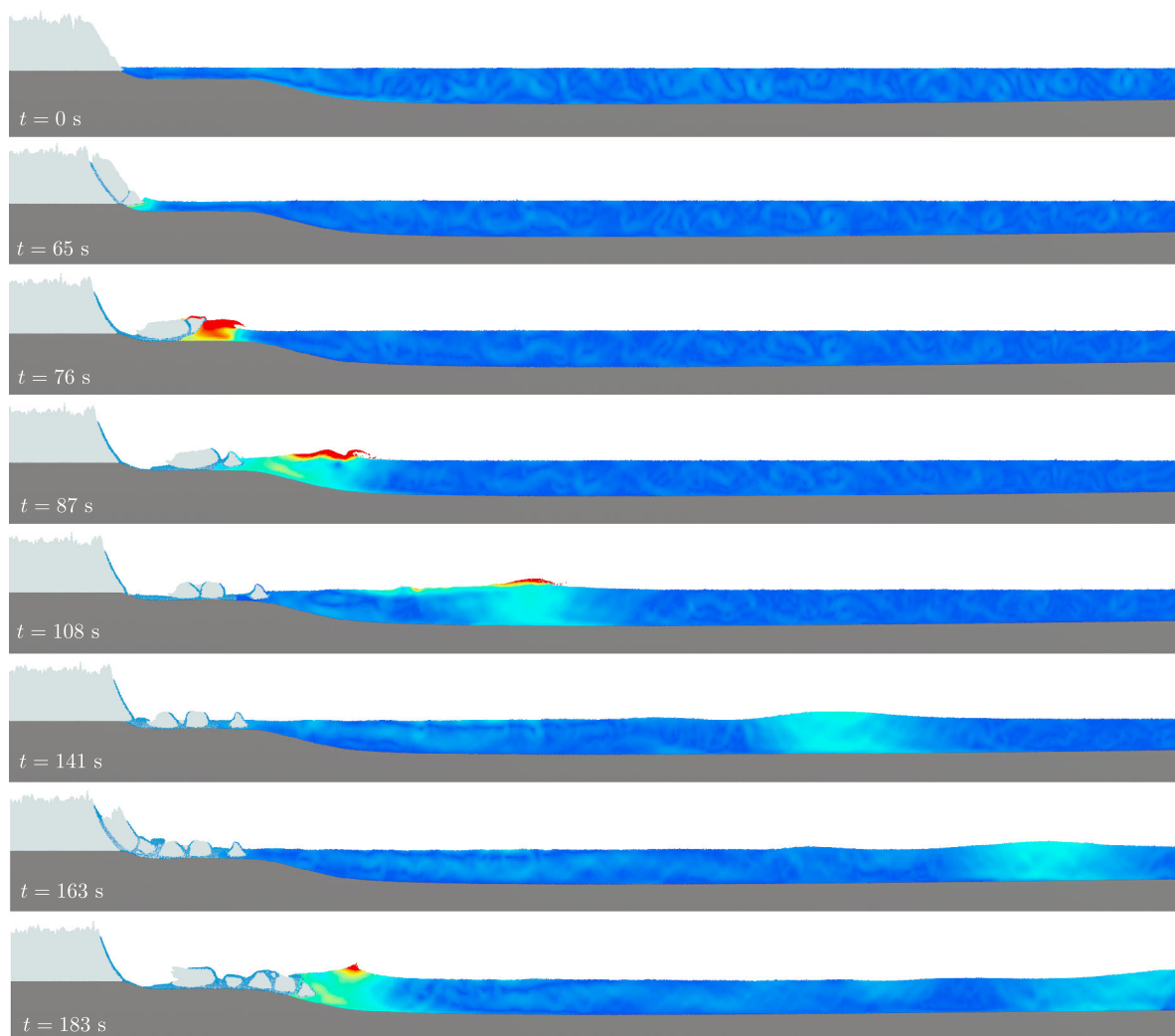
Calving-induced tsunami at the Eqip Sermia glacier. Given the ability of our model to quantitatively reproduce wave and ice fracture characteristics, we simulate one past calving event of the Eqip Sermia, a tidewater outlet glacier in Greenland, for which numerous observations and field measurements are available for both the glacier and tsunamis[10]. The geometry of the glacier front has been initialized according to the real shape of the glacier[10]. The undulating "crevassed" surface structure has been produced according to a Simplex Improved Perlin noise[35] to mimic the crevasse distribution of the glacier (Fig. 4 and Supplementary Movies 3 and 4). The detailed description of this event, the numerical setup, and the parameter calibration are given in the Methods. The failed portion of the glacier has a width of 75 m in our simulations which is slightly larger than the reported value measured between 50 and 60 m. The angle of the failure plane in our simulation is 54°, in good agreement with the measurements (between 45 and 60°). Note that the size of the initial iceberg is not only dependent on the relative water level, but also on the crevasse distribution, as shown in Fig. 4 where the failure is initiated at the location of the first deeper crevasse.

The wave amplitude measured in our MPM simulation (Fig. 4) 250 m from the calving front is 50 m, which is in good agreement with the wave amplitude observed at this location (between 45 and 50 m)[10]. A wave amplitude of 3.3 m was measured at the tide gauge on the shore opposite of the glacier. In our 2D simulation, the wave amplitude decreases from ~40 to 30 m at a distance of ~2000 m from the calving front and then slowly decreases further. We measure a wave amplitude of 27 m at the distance of the tide gauge, which corresponds to a wave amplitude between 2.5 and 6.6 m in 3D (see Methods) also in good agreement with the reported field measurement. Finally, we measure an average wave speed of 35 m/s, which also agrees well with the measured value

of 32 m/s; furthermore, this agrees with theoretical predictions for a fjord water depth estimated between 100 and 150 m[36], leading to a theoretical shallow-water velocity range between 31 and 38 m/s.

Discussion

We proposed a new model based on the MPM, a hybrid Eulerian-Lagrangian numerical technique, to simulate glacier calving and tsunami generation. Our nearly incompressible water model was able to reproduce well the effects of different iceberg calving mechanisms on the amplitude and speed of the generated tsunamis measured in laboratory experiments[13]. Deviations in maximum wave amplitude can be attributed to the empirical nature of the 2D/3D transformation (±50% deviation reported in Heller and Spinneken[34]). In addition, slight wave velocity deviations from the linear shallow-water limit theory can be attributed to the intermediate character and non-linearity of the waves as well as frequency dispersion for which variations around the linear wave theory expression can reach around ±10% for $a_w/D_w > 0.03$[37]. This wave velocity difference may contribute to the faster amplitude decrease in the gravity-dominated fall and capsizing cases. Our model is intended to simulate the complex multiphase interplay between ice and water mechanics during glacier calving. Although our water model has been extensively used in Smoothed Particle Hydrodynamics (SPH) free surface flow simulations of water and has been validated for several applications[32,38–40], solving incompressible Navier–Stokes equations using computational fluid dynamics would lead to more accurate results for the water dynamics[41]. Yet, it would also computationally be significantly more expensive and challenging to implement within the current hybrid solid-fluid numerical framework.

Fig. 4 MPM simulation of the Eqip Sermia glacier calving and tsunami generation and propagation. The water is colored by velocity: blue and red indicate water moving at 0 m/s and 20 m/s, respectively. The blue color in the glacier represents particles for which the yield criterion was met (plastic deformation). The ice cliff height is ~200 m and the water depth in the main fjord is ~125 m. Movies of this simulation can be found in the Supplement (Supplementary Movies 3 and 4).

Our new ice mechanical model has been validated by simulating a simple glacier calving geometry for which the competing effects of the glacier weight and buoyant forces lead to different ice fracture mechanisms and iceberg lengths that agreed well with theoretical predictions. When applying the model to a real-world outlet glacier, the model quantitatively reproduced the iceberg geometry and dimensions as well as the main characteristics of the generated tsunamis. The simulated iceberg length largely depends on the crevasse distribution and the chosen value of the ice's tensile strength. We back-calculated the latter such that the model results are in good agreement with the observations. Yet, we verified that the obtained value was within a realistic range based on extensive laboratory research on ice mechanics[28,42]. Nevertheless, glacial ice has high variability in its mechanical properties as well as deep crevasses leading to strong anisotropy, which both have not been accounted for here. In turn, one can expect smaller iceberg size distributions in reality[43] (see Supplementary Figs. 2 and 3). It is important to note that our model only applies to short time scales for which the ice behaves as a brittle material. We do not simulate viscous creep, nor the complex basal processes leading to crevasse formation. We could implement an ice creep law in our model, but the time-steps

required to capture fast ice fracture are incompatible with such slow, viscous deformations. However, one could easily couple the present model with a standard continuum glacier flow model[17,22]. In addition, note that an assumption in the formulation of our ice plastic flow rule gives rise to an analytical solution that speeds up simulation (see Supplementary Material and Simo[44]). This simplified formulation is based on the hypothesis of a relatively stiff material (see Eq. (5) in the Supplement), which is fully appropriate for ice. An iterative return mapping algorithm would be required for very soft matter (see Gaume et al.[27]).

The major advantage of our approach compared with existing methods[5,20,22,23] is the ability to simulate, in a unified manner, all of the processes related to fast glacier calving including dynamic ice fracture, tsunami formation, and propagation. In addition, we can apply our method to any type of geometry, including complex surface crevasses and boundary conditions. This allows us to analyze one or multiple subsequent calving events that can be measured, which is crucial for model validation. This unified and multiphysics approach prevents us from using model chains[5,8], which suffer from error propagation. Furthermore, the hybrid Eulerian-Lagrangian continuum framework leads to a tremendous reduction in the computational time compared with the
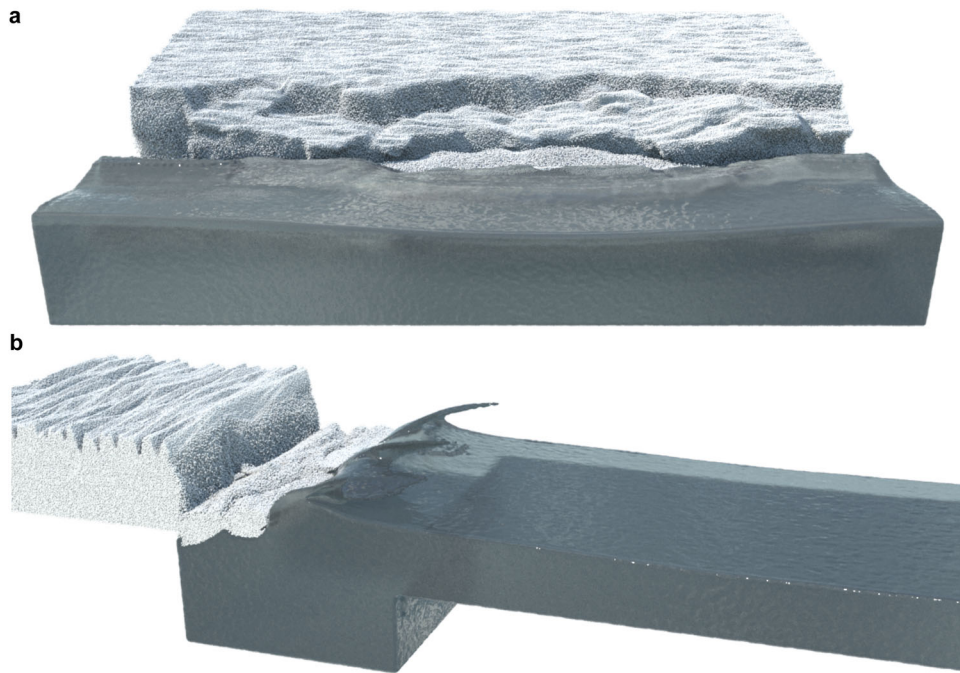
Fig. 5 Three-dimensional simulations of glacier calving and tsunami wave generation. a We simulate a wide glacier to focus on the 3D ice fracture characteristics. The ice cliff height is 150 m, the water depth is 200 m. The width of the system is 2 km, the glacier length is 1 km and the length of the water tank is 625 m. This simulation is composed of 36 million particles. A movie of this simulation can be found in the Supplement (Supplementary Movie 5). **b** Here, a long water tank is used to focus on the 3D tsunami propagation. The ice cliff height is 200 m and the water depth in the main fjord is 125 m. The width of the system is 400 m and the water tank is 1.6 km long. This simulation is composed of 20 million particles. A movie of this simulation can be found in the Supplement (Supplementary Movie 6).

discrete element method used in Astrom et al.[5]. For instance, 3D simulations (Fig. 5 and Supplementary Movies 5 and 6) of a single glacier calving event with 20–36 million particles takes <1 day on an office workstation (24 i9-9980XE CPU @ 3.00GHz, 128 Gb RAM). These advantages and the good agreements with laboratory and field data make our approach extremely well suited for glacier tsunami hazard assessment in coastal regions. Finally, our model can readily be applied to study lake outburst of glacial or mountain lakes induced by glacier calving[16], landslides, snow, ice, or rock avalanches[45–47].

Methods

A non-associative elastoplastic model for dynamic ice fracture. To model the dynamic hardening and softening of the glacial ice, we adapt and expand a non-associative elastoplastic model based on the aforementioned CCC yield surface used by Gaume et al.[27]. This yield surface showed great success for modeling the plasticity of snow by incorporating its natural cohesive properties; however, the previously chosen associative flow rule was only adequate owing to the porous nature of snow, allowing for some volume change. Conversely, in the case of a significantly less-porous material such as ice, choosing a non-associative flow rule is key owing to its natural volume-preserving qualities[30]. As such, we adopt the non-associative flow rule proposed by Wolper et al.[31] to model the dynamic fracture of a variety of solids while ensuring volume preservation. Unfortunately, this approach brings with it a unique problem in the discrete treatment of plasticity: when stresses are projected to the surface orthogonally to the hydrostatic axis, there is no change in pressure and, as such, no analytic way to compute the hardening/softening. Wolper et al. found success in treating this issue using a geometric intersection approach; however, we propose a more physically based approach that uses quantities we have analytic expressions for.

First, we outline the elastoplastic theory behind our return mapping approach. We use the deformation gradient, $\mathbf{F} = \partial\phi/\partial\mathbf{X}$, where $\phi(\mathbf{X}, t)$ denotes a deformation map from the undeformed coordinate $\mathbf{X}$ to the current configuration $\mathbf{x}$. Furthermore, we decompose $\mathbf{F}$ into an elastic part, $\mathbf{F}^E$, and a plastic part, $\mathbf{F}^P$, as $\mathbf{F} = \mathbf{F}^E\mathbf{F}^P$.

We adopt a split Neo-Hookean hyperelasticity model to predict nonlinear stress-strain relations suitable to simulating materials undergoing large deformations[48]; this deviatoric-dilational split energy allows for the separate penalization of shearing and volume change and is written as:

$$\Psi(\mathbf{F}) = \Psi^\mu(J^{\frac{-1}{d}}\mathbf{F}) + \Psi^\kappa(\mathbf{F}) \text{ so that } \Psi^\mu(\mathbf{F}) = \frac{\mu}{2}(\operatorname{tr}(\mathbf{F}^T\mathbf{F}) - d) \text{ and } \Psi^\kappa(J) = \frac{\kappa}{2}\left(\frac{J^2 - 1}{2} - \log(J)\right) \tag{2}$$

with $d = 2$ or 3 being the problem dimension, $J = \det(\mathbf{F})$, and μ and κ being the shear and bulk modulus, respectively. Using this model, we can also write out the Kirchoff stress, $\boldsymbol{\tau}$, and its deviatoric part, $\mathbf{s}$, as:

$$\boldsymbol{\tau} = \mu J^{\frac{-2}{d}}\operatorname{dev}(\mathbf{b}) + J\frac{\partial\Psi^K(J)}{\partial\mathbf{F}}\mathbf{I} = \mu J^{\frac{-2}{d}}\operatorname{dev}(\mathbf{b}) + J\Psi^{K'}(J)\mathbf{I} \tag{3}$$

$$\mathbf{s} = \operatorname{dev}(\boldsymbol{\tau}) = \mu J^{\frac{-2}{d}}\operatorname{dev}(\mathbf{b}) \tag{4}$$

Our yield surface is defined based on critical state soil mechanics[49] and depends on the first (pressure p) and second (Mises equivalent stress q) invariants of the Kirchoff stress tensor $\boldsymbol{\tau}$. We use the convention that compression corresponds to $p > 0$. Recent triaxial loading laboratory experiments showed that the yield surface of ice has an elliptical shape in the $p-q$ space[50]. As a consequence, we chose the following CCC yield surface similar to that used for snow by Gaume et al.[27] and Meschke et al.[51]:

$$y(p, q) = q^2(1 + 2\beta) + M^2(p + \beta p_0)(p - p_0) \tag{5}$$

where β is the cohesion coefficient, M is the slope of the cohesionless critical state line and p_0 is the pre-consolidation pressure. Softening or hardening is performed by shrinking or expanding the yield surface through variations in p_0 (Fig. 6). The major difference compared with Gaume et al.[27] is in the plastic flow rule and the hardening variable used for the hardening/softening relationship. Snow is a highly porous material, which justified the use of an associative plastic flow rule and a hardening law based on the volumetric plastic strain. In contrast, the failure of ice is not associated with large changes in volume[29]. Hence, a non-associative plastic flow rule has been developed, and a relevant formulation for the deviatoric plastic strain, α (see definition in Supplementary Note 1 and illustration in Supplementary Figure 1), is used in the hardening rule as follows:

$$p_0 = \kappa \sinh(\xi \max(-\alpha, 0)) \tag{6}$$

where $\kappa = \frac{2}{3}\mu + \lambda$ is the bulk modulus and ξ is the hardening factor. A q-based non-associative projection to the yield surface is performed if the trial elastic pressure p^{tr} is between $-\beta p_0$ and p_0. If this is not the case, projection is made to the tips of the yield surface (Fig. 6). The rate of deviatoric plastic deformation is positive ($\dot{\alpha} > 0$) if $p < p_c$, leading to material softening; conversely, the rate is
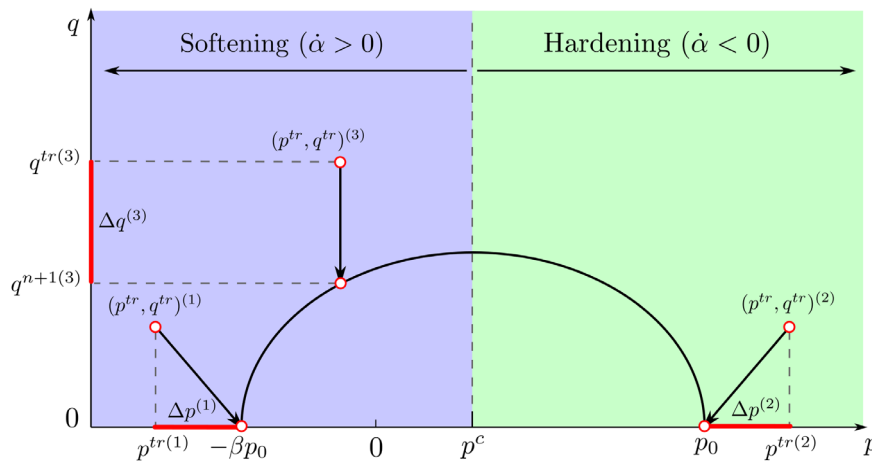
Fig. 6 Cohesive Cam Clay yield surface in the $p{-}q$ space to illustrate our new q-based hardening approach. Red points represent the $p{-}q$ state of a given particle before and after return mapping in each case (see Supplementary Note 1).

negative ($\dot{\alpha} < 0$) if $p > p_c$, inducing material hardening (see details in Supplementary Note 1). The proposed deviatoric hardening variable is also different from that proposed by Wolper et al.[31] who used a non-physically based variable formed from simple geometric considerations.

A nearly incompressible fluid model for water. Water is modeled as a nearly incompressible fluid[32] with stress tensor $\boldsymbol{\sigma}_w$ and partial stress p_w that depends on the current water density, ρ, and initial water density, ρ_w, according to:

$$\boldsymbol{\sigma}_w = -p_w \mathbf{1}, \quad p_w = \kappa_w \left(\left(\frac{\rho}{\rho_w} \right)^{\theta} - 1 \right) \tag{7}$$

where κ_w is the water bulk modulus and θ is a parameter that penalizes deviations from incompressibility. This relationship, which is classically used in water simulations using SPH, another particle-based method[32], is designed to stiffly prevent volume change of the water phase.

Material Point Method. MPM discretizes a continuum into Lagrangian material points to track mass, momentum, and deformation gradient, and uses a background Eulerian grid to solve mass and momentum conservation as follows:

$$\frac{D\rho}{Dt} + \rho \nabla \cdot \mathbf{v} = 0, \quad \rho \frac{D\mathbf{v}}{Dt} = \nabla \cdot \boldsymbol{\sigma} + \rho \mathbf{g} \tag{8}$$

where ρ is density, t is time, $\mathbf{v}$ is velocity vector, $\boldsymbol{\sigma}$ is the Cauchy stress tensor, and $\mathbf{g}$ is the gravitational acceleration vector. In MPM, mass is automatically conserved as the mass of each particle is constant. The momentum balance is solved on the background grid through discretization of its weak form. The explicit MPM algorithm by Stomakhin et al.[52] is applied with a symplectic Euler time integrator. Details of the adopted MPM time-stepping algorithm can be found in[27,52,53]. In contrast with Gaume et al.[27], we use the Affine Particle-In-Cell (APIC) method[54] to perform MPM transfer operations, which allows for better conservation of both linear and angular momentum.

The Cauchy stress tensor $\boldsymbol{\sigma}$ in Eq. (8) is related to the strain as follows

$$\boldsymbol{\sigma} = \frac{1}{J} \frac{\partial \Psi}{\partial \mathbf{F}_E} \mathbf{F}_E^T \tag{9}$$

where Ψ is the elastoplastic potential energy density, $\mathbf{F}_E$ is the elastic part of the deformation gradient, $\mathbf{F}$, and $J = \det(\mathbf{F})$.

Iceberg length theoretical model. Our choice to simulate glacier calving on a simple geometry is motivated by the existence of a simplified analytical solution for model validation. This solution has been derived based on the bending stresses induced by gravitational forces (from the interplay between the ice weight and buoyancy) using beam theory[55]. Ice fracture requires that the total bending stress induced by this interplay exceeds the ice's tensile strength, σ_t. Bending stresses can be computed according to $\sigma = Mz/I$ where M is the bending moment, z is the vertical coordinate (above the neutral surface), and I is the moment of inertia. This leads to the following instability criterion:

$$\left| \underbrace{\frac{3\rho_i g L_i^2}{2H_i}}_{\text{ice weight}} - \underbrace{\frac{3\rho_w g L_i^2}{2D}}_{\text{buoyancy}} \right| = \sigma_t \tag{10}$$

which leads to Eq. (1).

Table 1 Experimental parameters of the three selected laboratory experiments of Heller et al.[13].

Block parameters	GF	BF	CS
Block length (m)	0.5	0.5	0.8
Block thickness s (m)	0.5	0.5	0.25
Block width b (m)	0.8	0.8	0.5
Block volume $\Forall_s$ (m³)	0.2	0.2	0.1
Block density ρ_s (kg/m³)	936	923	924
Block mass m_s (kg)	187.1	184.6	92.4
Water depth D_w (m)	1	1	1
Release position of block base from the still water surface (m)	0.00	−0.83	−0.74
Block velocity v_s (m)	1.15	0.48	0.61
Froude number F	0.37	0.15	0.19
Relative block thickness S	0.5	0.5	0.25
Relative block mass M	0.23	0.23	0.18

Experimental data

2D/3D transformation. The general expression for the transformation of the 2D to 3D primary wave amplitudes is given by Heller and Spinneken[34]:

$$\frac{a_{3D}}{a_{2D}} = 1.5 \left[\left(\frac{r}{D_w} F^{-0.40} S^{-0.50} M^{-0.50} \right) \right]^{-5/6} f_\gamma \tag{11}$$

where r is the radial distance from the impact, D_w is the water depth, γ is the wave propagation angle, and the parameters F, S, and M are the slide Froude number, the relative slide thickness, and the relative slide mass, respectively, and defined as follows:

$$F = \frac{v_s}{\sqrt{g D_w}}, \quad S = \frac{s}{D_w}, \quad M = \frac{m_s}{\rho_w b D_w^2}, \tag{12}$$

where v_s is the slide velocity, s is the slide thickness, m_s is the slide mass, and b is the slide width. The function f_γ is defined as

$$f_\gamma = \cos^{2(1 + \exp[-0.2(r/D_w)])}(2\gamma/3) \tag{13}$$

Iceberg-tsunami laboratory experiments. We conducted the experiments in the Delta Basin of Deltares, Delft, with effective size, excluding wavemakers and absorbing beaches, of 40.3 m × 33.9 m. The total number of experiments was 66. The following provides an overview of the three herein selected experiments with further details for all experiments given by Heller et al.[13,37].

Table 1 shows the relevant parameters. We modeled the icebergs with polypropylene homopolymer blocks with a density similar to that of ice. The 0.500 m × 0.800 m × 0.500 m block in the gravity- and buoyancy-dominated fall cases was released at the vertical boundary of the basin and the 0.500 m × 0.800 m × 0.250 m block in the capsizing case was released offshore. The blocks weighed up to 187.1 kg and the still water depth was 1.00 m.

Three types of experiments were conducted: (i) GF, (ii) BF, and (iii) CS. For GF cases, we held the block in position with an electromagnet prior to release, which was connected to a rope. We fixed the supporting frame for this electromagnet and the block to a steel plate at the basin wall. The block was moved in the vertical
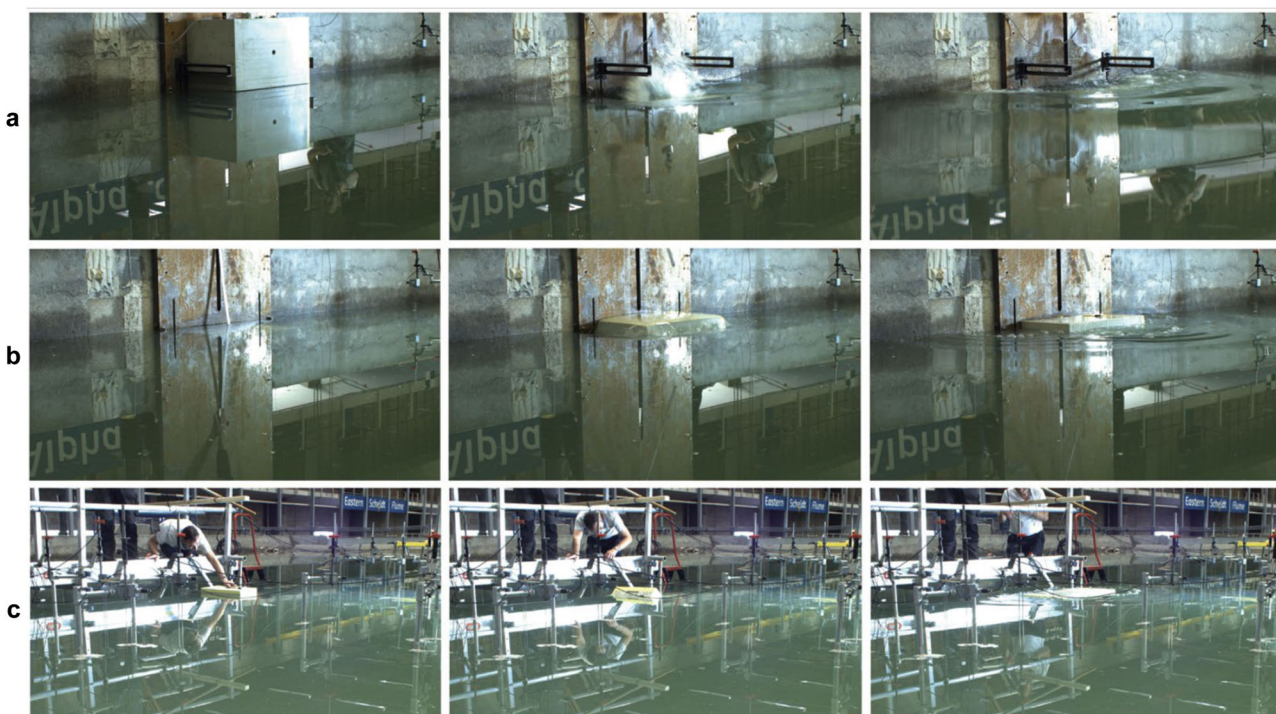
Fig. 7 Pictures of the laboratory experiments. a Gravity-dominated fall; **b** Buoyancy-dominated fall; **c** capsizing. From Heller et al.[13].

Table 2 Numerical and mechanical parameters used in the simulations.

Case	Δx (m)	N_p	ρ_i (kg/m³)	E_i (GPa)	ν_i	ρ_w (kg/m³)	Water model (κ (MPa), θ)	NACC (βp_0 (MPa), ξ, M)
Tsunami laboratory (Fig. 2)	0.01	640 k	920	-	-	1000	(10, 7)	-
Simple geometry (Fig. 3)	$H_i/40$	55 k–79 k	900	1	0.3	1000	(10, 7)	(0.5, 3, 1.4)
Tsunami Eqip Sermia (Fig. 4)	2.5	370 k	900	1	0.3	1000	(10, 7)	(0.8, 0.1, 0.13)
3D calving 1 (Fig. 5a)	5	36 M	900	10	0.3	1000	(10, 7)	(2, 3, 1.4)
3D calving 2 (Fig. 5b)	5	20 M	900	0.1	0.3	1000	(10, 7)	(0.5, 3, 1.4)

direction towards the release position using a winch system fixed to a support structure outside the basin. For BF cases, the block was pulled underwater to the release position with a rope attached to the center of the block base. We further stabilized the block with a steel beam from above (Fig. 7) and released both the beam and the rope simultaneously to initiate waves.

For CS cases, we held the block in position with a wooden rod guided through the center of the block. Steel profiles on both sides accommodated this rod such that the block was able to heave and pitch, but not to sway and surge. We initiated capsizing by removing a fitting that stabilized the block and then simply releasing the block by hand (Fig. 7).

The velocity v_s corresponds to the fastest moving section of the block derived from the recordings of a nine Degree of Freedom motion sensor (Adafruit BNO055) with a procedure described in Chen et al.[26]. The sensor was located in a watertight enclosure and attached to the block surface. We extracted the still images shown in Fig. 7 from camera footage recorded with a 5 MP PointGrey ZBR2-PGEHD-50S5C-CS camera at 15 Hz. We used up to 35 resistance-type wave probes to record the wave features. Relative to the coordinate origins at the front of the steel plate in the center of the block in the cross-shore direction (GF and BF cases) and at the block center (CS case), we arranged these probes at different points in the range of relative radial distances $r/D_w = 2$–35 and wave propagation angles $\gamma = 0°$ (block axis) to $-75°$ (fall cases) and $r/D_w = 2$–15 and $\gamma = 0°$ to $-180°$ (capsizing case). The angle γ is thereby defined positively in the clockwise direction. We shortened the water surface time series individually to remove data affected by reflection from the basin boundaries and filtered most wave probe data with a low-pass filter with a cutoff frequency at 9–11 Hz[37].

Eqip Sermia glacier calving—tsunami field experiments. Glacier calving activity at Eqip Sermia was investigated with a terrestrial radar interferometer (TRI), surveys with unmanned aerial vehicles (drones), pressure sensors, and time-lapse cameras[56]. The ice wall collapse and the ensuing tsunami were filmed by tourists on a tour boat. The exact thickness of removed ice was determined at high spatial resolution (10 m pixel size) from TRI interferograms, as was the terminus geometry before, during and after the collapse (Lüthi and Vieli[10]). The position of the tour

boat was registered with the TRI, such that the tsunami wave height from the videos could be geometrically determined. The wave height in the impact zone on the shore opposite of the glacier was registered with a pressure sensor at a 4 s interval.

Concerning the 2D/3D transformation, the following ranges of F, S, and M have been used[10] in the article:

$$F_{\text{GF}} = 2.1 - 3 , \quad S_{\text{GF}} = 1.5 - 2.5 , \quad M_{\text{GF}} = 5 - 20 \qquad (14)$$

Setup of the simulations. In all our simulations, the resolution of the MPM background mesh was chosen 40–50 times smaller than the minimum characteristic geometrical length of the system (rigid block length, glacier height, or water depth). In 2D and 3D simulations, we used approximately four and eight material points per element, respectively. In addition, the time step was evaluated based on both the CFL and elastic wave speeds to ensure the stability of the simulation.

Tsunami (Fig. 2). A 2D water tank of $16 \text{ m} \times 1 \text{ m}$ is simulated. For GF and BF simulations, a solid block of $0.5 \text{ m} \times 0.5 \text{ m}$ is used. In the GF experiment, the block is released on the left side of the tank with the bottom at the level of the water's free surface. For the BF case, the block is released with the bottom at a depth of -0.83 m corresponding to the experimental setup (Table 1). For the CS simulation, a solid block of $0.8 \text{ m} \times 0.25 \text{ m}$ is used and released from a neutrally floating position with an initial angle of 35° to activate capsizing in a similar way as in the experiments (small initial movement by hand). For all cases, we use a block density of 920 kg/m³ (similar to that of ice). The numerical and mechanical parameters are presented in Table 2.

Effect of buoyancy on iceberg lengths (Fig. 3). A 2D water tank of length $250 \times N$ m and depth $50 \times N + D_w$ m is simulated with $N \in \{1, 3, 5, 10\}$. The ice slab has a length of $150 \times N$ m and a cliff height of $H_i = N \times 40$ m. The ice slab slides on a frictionless boundary condition with a speed of $1 \times \sqrt{N}$ m/s. Simulations are performed with a constant water level, i.e., the water level increase due to iceberg generation is compensated by water particles exiting the water tent at the water

tank outlet. The water tank has frictionless walls. The numerical and mechanical parameters are presented in Table 2. In this case, generic mechanical properties falling within a realistic range of reported values for ice[28] were chosen for the sake of the comparison with the analytical model. An elastic modulus of 1 GPa was chosen following Astrom et al.[5,20].

Calving-induced tsunami at the Eqip Sermia glacier (Fig. 4). We simulated a 2D water tank of length 4500 m with variable depth. The first 500 m of the fjord have an average depth of 35 m and smoothly increases to a depth of ~135 m in the main fjord, in agreement with field observations[10]. The ice cliff is 200 m high and the real-world shape of the calving ice mass measured in Lüthi and Vieli[36] has been modeled. The crevasse distribution has been simulated according to the Perlin simplex terrain noise model[35] leading to surface crevasses typically between 20 and 50 m deep and crack openings between 5 and 10 m. Parameters are presented in Table 2. In this case, model parameters were back-calculated within a range of realistic values for ice[28,42] to achieve good agreement (iceberg size and failure angle) with observations. An elastic modulus of 1 GPa was chosen following Astrom et al.[5,20].

3D glacier calving (Fig. 5a). We simulated a glacier that is 1 km long, 2 km wide and has a 150 m irregular vertical cliff. The water tank is 200 m deep. The submergence depth is 40 m corresponding to $H_i/D \sim 0.26$. The glacier is supported by a frictionless base that slides backward at a speed of 3 m/s, in order to progressively remove basal support at the calving front and thus induce calving. Initial cracks have been placed within the glacier to mimic crevasses. These initial cracks follow a Voronoi distribution with cell size $\mathbf{r} = (30, 80, 160)$ m. Parameters are presented in Table 2. Generic yield surface parameters were chosen in agreement with experimental data[28]. Concerning the elastic modulus, most studies related to glacier calving numerical simulations use elastic moduli for ice lower than experimentally measured values to speed up simulation[5,20] (as the time step depends on the elastic wave speed). In this simulation, to test the capabilities of our model in simulating large-scale calving events with realistic properties, we used an elastic modulus of $E = 10$ GPa based on experimentally measured values[42].

3D glacier calving and tsunami generation (Fig. 5b). We simulated a water tank of variable depth: the first 500 m are 300 m deep, and then the next 1250 m are 135 m deep. The ice slab is 600 m long and has a 200 m irregular vertical cliff. The crevasse distribution is the same as in the Eqip Sermia 2D simulation. The submergence depth is 50 m corresponding to $H_i/D \sim 0.2$. The glacier slides over a frictionless boundary condition at a speed of 3 m/s. Parameters are presented in Table 2. In this case, a low elastic modulus value was chosen to speed up the simulation (which suffers from the large size of the water tank). Generic values of the yield surface parameters were chosen within a realistic range[28,42]. An elastic modulus of 0.1 GPa was chosen following Astrom et al.[20] to speed up this simulation and focus on tsunami characteristics.

Data availability

The data corresponding to the iceberg-tsunami laboratory experiments can be found at https://hydralab.eu/research--results/ta-projects/project/hydralab-plus/11/. The data corresponding to the Eqip Sermia glacier calving—tsunami field experiments can be found in a previous publication at https://tc.copernicus.org/articles/10/995/2016/.

Code availability

The CD-MPM code is open-access and available on GitHub at the following address: https://github.com/penn-graphics-research/ziran2019.

References

1. Moore, J. C., Grinsted, A., Zwinger, T. & Jevrejeva, S. Semiempirical and process-based global sea level projections. *Rev. Geophys.* **51**, 484–522 (2013).
2. Catania, G., Stearns, L., Moon, T., Enderlin, E. & Jackson, R. Future evolution of Greenland's marine-terminating outlet glaciers. *J. Geophys. Res. Earth Surf.* **125**, e2018JF004873 (2020).
3. Pattyn, F. & Morlighem, M. The uncertain future of the Antarctic ice sheet. *Science* **367**, 1331–1335 (2020).
4. Rignot, E., Velicogna, I., van den Broeke, M. R., Monaghan, A. & Lenaerts, J. T. Acceleration of the contribution of the Greenland and Antarctic ice sheets to sea level rise. *Geophys. Res. Lett.* **38**, L05503(2011).
5. Aström, J. A. et al. Termini of calving glaciers as self-organized critical systems. *Nat. Geosci.* **7**, 874 (2014).
6. Benn, D. I., Warren, C. R. & Mottram, R. H. Calving processes and the dynamics of calving glaciers. *Earth-Sci. Rev.* **82**, 143–179 (2007).
7. Benn, D. I. et al. Melt-under-cutting and buoyancy-driven calving from tidewater glaciers: new insights from discrete element and continuum model simulations. *J. Glaciol.* **63**, 691–702 (2017).
8. Benn, D. I. & Aström, J. A. Calving glaciers and ice shelves. *Adv. Phys* **3**, 1513819 (2018).
9. Reeh, N. Long calving waves. In *POAC'85, 8th International Conference on Port and Ocean Engineering Under Arctic Conditions* (1985).
10. Lüthi, M. P. & Vieli, A. Multi-method observation and analysis of a tsunami caused by glacier calving. *Cryosphere* **10**, 995–1002 (2016).
11. MacAyeal, D. R., Abbot, D. S. & Sergienko, O. V. Iceberg-capsize tsunamigenesis. *Ann. Glaciol.* **52**, 51–56 (2011).
12. Levermann, A. When glacial giants roll over. *Nature* **472**, 43–44 (2011).
13. Heller, V. et al. Large-scale experiments into the tsunamigenic potential of different iceberg calving mechanisms. *Sci. Rep.* **9**, 1–10 (2019).
14. Mikkelsen, N. & Ingerslev, T. *Nomination of the Ilulissat Icefjord for inclusion in the World Heritage List* (Geological Survey of Denmark and Greenland, 2003).
15. Huge iceberg threatens tiny Greenland village. *The Guardian* (2018). Https://www.theguardian.com/world/2018/jul/14/huge-iceberg-threatens-village-in-greenland.
16. Clague, J. J. & O'Connor, J. E. Glacier-related outburst floods. In *Snow and ice-related hazards, risks and disasters* (Elsevier, 2020).
17. Gagliardini, O. et al. Capabilities and performance of elmer/ice, a new-generation ice sheet model. *Geosci. Model Dev.* **6**, 1299–1318 (2013).
18. Bassis, J. & Walker, C. Upper and lower limits on the stability of calving glaciers from the yield strength envelope of ice. *Proc. R. Soc. A* **468**, 913–931 (2012).
19. Amaral, T., Bartholomaus, T. & Enderlin, E. Evaluation of iceberg calving models against observations from Greenland outlet glaciers. *J. Geophys. Res. Earth Surf.* **125**, e2019JF005444 (2019).
20. Aström, J. et al. A particle based simulation model for glacier dynamics. *Cryosphere* **7**, 1591-1602 (2013).
21. Bassis, J. N. & Jacobs, S. Diverse calving patterns linked to glacier geometry. *Nat. Geosci.* **6**, 833–836 (2013).
22. Mercenier, R., Lüthi, M. P. & Vieli, A. A transient coupled ice flow-damage model to simulate iceberg calving from tidewater outlet glaciers. *J. Adv. Model. Earth Syst.* **11**, 3057–3072 (2019).
23. Mercenier, R., Lüthi, M. & Vieli, A. How oceanic melt controls tidewater glacier evolution. *Geophys. Res. Lett.* **47**, 2019GL086769 (2020).
24. Heller, V., Hager, W. H. & Minor, H.-E. Landslide generated impulse waves in reservoirs: basics and computation. *VAW-Mitteilungen* **211** (2009).
25. Evers, F., Heller, V., Fuchs, H., Hager, W. H. & Boes, R. Landslide-generated impulse waves in reservoirs: basics and computation. 2nd edn, *VAW-Mitteilungen* **254** (2019).
26. Chen, F., Heller, V. & Briganti, R. Numerical modelling of tsunamis generated by iceberg calving validated with large-scale laboratory experiments. *Adv. Water Resour.* **142**, 103647 (2020).
27. Gaume, J., Gast, T., Teran, J., van Herwijnen, A. & Jiang, C. Dynamic anticrack propagation in snow. *Nat. Commun.* **9**, 3047 (2018).
28. Derradji-Aouat, A. Multi-surface failure criterion for saline ice in the brittle regime. *Cold Reg. Sci. Technol.* **36**, 47–70 (2003).
29. Ringeisen, D., Tremblay, L. B. & Losch, M. Non-normal flow rules affect fracture angles in sea ice viscous-plastic rheologies. *The Cryosphere Discussions* 1–24 (2020).
30. Rist, M. & Murrell, S. Ice triaxial deformation and fracture. *J. Glaciol.* **40**, 305–318 (1994).
31. Wolper, J. et al. CD-MPM: continuum damage material point methods for dynamic fracture animation. *ACM Trans. Graph.* **38**, 4 (2019).
32. Becker, M. & Teschner, M. Weakly compressible SPH for free surface flows. In *Proc ACM SIGGRAPH/Eurograph Symp Comp Anim*, 209–217 (2007).
33. Sulsky, D., Chen, Z. & Schreyer, H. L. A particle method for history-dependent materials. *Comp. Methods Appl. M* **118**, 179–196 (1994).
34. Heller, V. & Spinneken, J. On the effect of the water body geometry on landslide–tsunamis: physical insight from laboratory tests and 2d to 3d wave parameter transformation. *Coast. Eng.* **104**, 113–134 (2015).
35. Perlin, K. Improving noise. In *ACM Transactions on Graphics (TOG)*, **21**, 681–682 (ACM, 2002).
36. Lüthi, M. P. et al. A century of geometry and velocity evolution at Eqip Sermia, West Greenland. *J. Glaciol.* **62**, 640–654 (2016).
37. Heller, V., Attili, T., Chen, F., Gabl, R. & Wolters, G. Large-scale investigation into iceberg-tsunamis generated by various iceberg calving mechanisms. *Coast, Eng.* **163**, 103745 (2021).
38. Dao, M., Xu, H., Chan, E. & Tkalich, P. Numerical modelling of extreme waves by smoothed particle hydrodynamics. *Nat. Hazards Earth Syst. Sci.* **11**, 419 (2011).
39. Xu, X. An improved SPH approach for simulating 3d dam-break flows with breaking waves. *Comput. Methods Appl. M.* **311**, 723–742 (2016).

40. Shao, J., Yang, Y., Gong, H. & Liu, M. Numerical simulation of water entry with improved SPH method. *Int. J. Comput. Methods* **16**, 1846004 (2019).

41. Yavari-Ramshe, S. & Ataie-Ashtiani, B. Numerical modeling of subaerial and submarine landslide-generated tsunami waves-recent advances and future challenges. *Landslides* **13**, 1325–1368 (2016).

42. Petrovic, J. J. Review mechanical properties of ice and snow. *J. Mater. Sci.* **38**, 1–6 (2003).

43. Gaume, J. et al. Evaluation of slope stability with respect to snowpack spatial variability. *J. Geophys. Res.* **119**, 1783–1789 (2014).

44. Simo, J. C. A framework for finite strain elastoplasticity based on maximum plastic dissipation and the multiplicative decomposition: Part i. continuum formulation. *Comput. Methods Appl. M.* **66**, 199–219 (1988).

45. Naaim, M. Impulse water waves generated by snow avalanches. In *International Snow Science Workshop (ISSW)*, pp–619 (Irstea, ANENA, 2013).

46. Zitti, G., Ancey, C., Postacchini, M. & Brocchini, M. Impulse waves generated by snow avalanches: momentum and energy transfer to a water body. *J. Geophys. Res. Earth Surf.* **121**, 2399–2423 (2016).

47. Zitti, G., Ancey, C., Postacchini, M. & Brocchini, M. Snow avalanches striking water basins: behaviour of the avalanche's centre of mass and front. *Nat. Hazards* **88**, 1297–1323 (2017).

48. Yue, Y. et al. Hybrid grains: Adaptive coupling of discrete and continuum simulations of granular media. In *SIGGRAPH Asia 2018 Technical Papers*, SIGGRAPH Asia '18, 283:1–283:19 (2018).

49. Schofield, A. & Wroth, P.*Critical state soil mechanics* (McGraw-Hill, 1968).

50. Zhou, Z. et al. Yield surface evolution for columnar ice. *Results Phys.* **6**, 851–859 (2016).

51. Meschke, G., Liu, C. & Mang, H. A. Large strain finite-element analysis of snow. *J. Eng. Mech.* **122**, 591–602 (1996).

52. Stomakhin, A., Schroeder, C., Chai, L., Teran, J. & Selle, A. A material point method for snow simulation. *ACM Trans. Graph.* **32**, 102:1–102:10 (2013).

53. Jiang, C., Schroeder, C., Teran, J., Stomakhin, A. & Selle, A. The material point method for simulating continuum materials. In *ACM SIGGRAPH 2016 Course*, 24:1–24:52 (2016).

54. Jiang, C., Schroeder, C. & Teran, J. An angular momentum conserving affine-particle-in-cell method. *J. Comput. Phys.* **338**, 137–164 (2017).

55. Timoshenko, S. & Goodier, J.*Theory of Elasticity*, **37** (McGraw-Hill, 1970).

56. Walter, A., Lüthi, M. P. & Vieli, A. Calving event size measurements and statistics of Eqip Sermia, Greenland, from terrestrial radar interferometry. *Cryosphere* **14**, 1051–1066 (2020).

Author contributions

J.W. developed the non-associative elastoplastic model and wrote the corresponding methods section under the supervision of C.J., J.G., and M.G. The MPM code and the APIC transfer scheme was developed by C.J. The field experiments at the Eqip Sermia glacier were performed by M.L. and A.V. who provided expertise on glacier calving processes. V.H. performed the tsunami laboratory experiments and advised on calving-induced tsunamis. J.W., M.G., and J.G. performed the simulations. J.G. obtained the collaborating funds, designed the study and wrote the paper with J.W. and essential inputs from all co-authors.

Competing interests

The authors declare no competing interests.

Additional information

Supplementary information The online version contains supplementary material available at https://doi.org/10.1038/s43247-021-00179-7.

Correspondence and requests for materials should be addressed to J.G.

Peer review information Primary handling editor: Joseph Aslin.

Reprints and permission information is available at http://www.nature.com/reprints

Publisher's note Springer Nature remains neutral with regard to jurisdictional claims in published maps and institutional affiliations.